International Communications in Heat and Mass Transfer 79 (2016) 58–66

Contents lists available at ScienceDirect

International Communications in Heat and Mass Transfer

journal homepage: www.elsevier.com/locate/ichmt

A three-dimensional lattice Boltzmann model for numerical investigation of bubble growth in pool boiling☆

Reza Sadeghi [a], Mostafa Safdari Shadloo [b,*], Mohammad Yaghoub Abdollahzadeh Jamalabadi [c], Arash Karimipour [d]

[a] Department of Mechanical Engineering, University of Tehran, Tehran, Iran
[b] CORIA-UMR 6614, Normandie University, CNRS-University & INSA of Rouen, 76000 Rouen, France
[c] Department of Mechanical, Robotics and Energy Engineering, Dongguk University, Seoul 04620, Republic of Korea
[d] Department of Mechanical Engineering, Najafabad Branch, Islamic Azad University, Najafabad, Iran

ARTICLE INFO

Available online 25 October 2016

Keywords:
Lattice Boltzmann method
Pool boiling
Bubble departure diameter
Jacob number
Surface tension
Gravity acceleration

ABSTRACT

In this paper, a three-dimensional lattice Boltzmann model is proposed to simulate pool-boiling phenomena at high-density ratios. The present model is able to predict the temperature field inside the bubble. The three-dimensional multiphase model is validated against the analytical solution of evaporation d^2law problem and Laplace's law. In addition, effects of different parameters including, Jacob number, gravitational acceleration (g) and surface tension (σ) on bubble departure diameter are presented for further validation. The bubble departure diameter is found to be proportional to $g^{-0.354}$ and $\sigma^{0.5}$, and has a linear relation with Jacob number. These results are more consistent with previous experimental correlations when compared with available lattice Boltzmann literature. Furthermore, the dynamic behavior of multiple bubble formation sites such as micro convection and vortex ring mechanism are presented to show the capability of presented model for capturing more complex physical phenomena. To sum up, the proposed three-dimensional lattice Boltzmann model is feasible and accurate for numerical simulations of pool boiling.

© 2016 Elsevier Ltd. All rights reserved.

1. Introduction

Boiling is one of the most important phenomena that occur in various industrial fields. Pool boiling happens when the heating surface is submerged in a large body of stagnant liquid. Although a great number of experimental works have been performed to study boiling during the past century, its theory is rather complex and not yet fully understood. Recently by the advancement of computer technologies and the development of numerical simulations, many techniques have been developed to simulate pool-boiling phenomenon.

Pool boiling is a complicated multiphase process. Multiphase flows occur when two or more fluids are in the vicinity of each other while sharing an interface. To simulate multiphase flows, precise representation of the interface and capturing its topological changes, several macroscopic methods have been developed so far. This includes, but not limited to front-tracking method [1], volume of fluid (VOF) [2,3], level set method [4], and smoothed particle hydrodynamics [5,6], among others. A comprehensive recent review on available techniques and their advantages and disadvantages can be found in [7,8].

In recent years, lattice Boltzmann method (LBM) became a popular tool to simulate physical phenomena [9]. LBM has great potentials in modeling multiphase flows and appears to be an effective tool for simulation of the problems that involve complex boundaries and interfacial dynamics [10]. Compared to traditional computational fluid dynamics (CFD) methods, LBM has many advantages such as easy programming and parallelizing. Besides, in this method, it is not necessary to solve the poison equation for the pressure field. Thus, LBM can be much faster than common CFD methods.

Several LBM models have been developed to simulate multiphase flows. Among others one can mention, color-gradient model [11], Shan-Chan model [12], free-energy model [13], finite difference LBM [14] and HZN interface tracking model [15]. It is noted that all of these pioneering works have limitations in the simulation of interfacial flows with high-density ratios. To overcome such shortcomings several new models have been proposed in the last decade. For instance, Inamaru et al. [16] developed a new free-energy model which can track the interface by applying a diffuse equation which is analogy to the Cahn–Hilliard (C–H) equation. Although they achieved high-density ratios, the computation load of their model was heavy due to

☆ Communicated by J. Taine and A. Soufiani.

* Corresponding author.
E-mail address: msshadloo@coria.fr (M.S. Shadloo).

http://dx.doi.org/10.1016/j.icheatmasstransfer.2016.10.009
0735-1933/© 2016 Elsevier Ltd. All rights reserved.

solving the poison equation. Zheng et al. [17] developed a Galilean-invariant free-energy model which is simpler to the Inamaru's model and does not require pressure correction as before. Lee [18] proposed a new model, based on HCZ interface tracking model [15], to handle the multiphase problems with high-density ratios. In the Lee's model, intermolecular forces are expressed in the potential forms and the parasitic current, which is initiated with truncation errors of interfacial stresses, is eliminated. Safari and Rahimyan [19] developed a model based on phase-field lattice Boltzmann approach of Lee & Lin [20]. They extend the Lee & Lin model by adding a suitable equation to account for the finite divergence of the velocity field within the interface region. Furthermore, the convective Cahn-Hilliard equation is extended to take into account vaporization effects. This model was successfully validated for varies problems including high-density ratio condensations and evaporations (see [21–23]).

Besides above-mentioned works, some researchers studied the simulation of pool boiling by LBM. Yang et al. [24] investigated transition mechanism in boiling regime by using the Shan & Chen [12] multiphase model on vertical and horizontal surfaces. The density ratio reported in this work was limited to low density ratios. Ryu & Ko [25] performed the free energy based multiphase LBM to simulate the pool boiling. Gong & Cheng [26] simulated the bubble growth and departure from a horizontal surface by using modified pseudo-potential model. More recently, Li et al. [27] utilized a thermal pseudopotential LB model for simulating liquid-vapor boiling process. They simulated three boiling stages (nucleate, transition, and film boiling) as well as the boiling curve. Zhiqiang et al. [28] simulated the bubble growth and its departure from a superheated wall with an improved hybrid LBM. Sun & Li [29] investigated three-dimensional pool boiling from a horizontal heated wall using a hybrid LBM. Although, according to the thermal interferometric pattern presented by Beer [30] the temperature inside a growing and rising vapor bubble varies in time, in the models utilized in these works, the temperature field inside the bubble were assumed to be constant in these works. Satari et al. [31] simulated the pool boiling phenomenon by using the combination of three-dimensional isothermal and two-dimensional non-isothermal models. A recent review of the applications of LB methods for thermal flows and thermal multiphase flows with phase change can be found in [32].

As it can be seen from these works, most of the available literatures are limited to either low-density ratio models, or the temperature field is either neglected or miscalculated especially for three-dimensional pool boiling case. Therefore, in this paper, the modified Lee model is extended and a three-dimensional LBM is proposed to simulate pool boiling with high-density ratios on horizontal superheated walls. The code is validated by three-dimensional droplet evaporation, Laplace's law and evaporation d^2 law problems. The process of the bubble growth and its topology found to be in good agreement with available literature. Effects of gravitational acceleration, surface tension and Jacob number on the bubble departure diameter in three-dimensional model are also compared with experimental correlations where it is found that the presented model is in better agreement with these correlations when compared with available LBM results. Additionally, the simulations are extended for multi-bubble growth to show the capability of current three-dimensional model in capturing more complex physics.

2. Numerical model

In this section we introduce the extended model of Lee [18] with considering the phase change by incorporating a source term at the three-dimensional phase interface. This model is originally presented by Safari and Rahimian [19] for two-dimensional phase change phenomena and is extended to three-dimension in this work for the first time according to the authors' best knowledge.

2.1. Governing equation

Considering the system of two incompressible and immiscible fluids with different densities and viscosities, the continuity equation of Cahn-Hilliard in the presence of phase change can be written as:

$$\frac{\partial \tilde{\rho}_i}{\partial t} + \nabla . q_i = \pm \dot{m}''', \tag{1}$$

where $\tilde{\rho}_i$ is the local density of the component i (vapor or liquid phase), t is time, q_i and $\dot{m}'''$ denote the mass flow rate per unit volume of component i and the volumetric mass source term for evaporation, respectively ($q_i = \tilde{\rho}_i u$ and u is the volumetric flow averaged velocity). In regions close to the interface, the total mass flow rate of each component is affected by the diffusive mass flow, which is indicated by $\rho_i j_i$. Therefore, the volume diffusive flow rate, j_i, for ith component read as:

$$\rho_i j_i = \tilde{\rho}_i (u_i - u), \tag{2}$$

where u_i and ρ_i are the volumetric flow averaged velocity and density of the phase i (vapor or liquid phase). Thus, at the interface, the total mass flow of component i expresses as:

$$q_i = \tilde{\rho}_i u - \rho_i j_i. \tag{3}$$

The local averaged density (ρ) is a function of local densities (vapor or liquid component):

$$\rho = C\rho_l + (1-C)\rho_v, \tag{4}$$

where $C = \tilde{\rho}_l / \rho_l$ is the liquid phase composition, and ρ_l and ρ_v are the local densities of the liquid and vapor phases, respectively. Note that the subscripts l and v are used for distinguishing between liquid and vapor phases, receptively, in the rest of this manuscript. The Cahn-Hilliard continuity equation (Eq. (1)) is, therefore, separated to two equations for either component:

$$\frac{\partial C}{\partial t} + \nabla \cdot (uC) - \nabla \cdot j_l = -\frac{\dot{m}'''}{\rho_l}, \tag{5}$$

$$\frac{\partial (1-C)}{\partial t} + \nabla \cdot (u(1-C)) - \nabla \cdot j_v = -\frac{\dot{m}'''}{\rho_v}. \tag{6}$$

Since $j_l = -j_v$, the divergence of the velocity field within the interface is obtained by summing Eqs. (5) and (6) as follows:

$$\nabla . u = \dot{m}''' \left(\frac{1}{\rho_v} - \frac{1}{\rho_l} \right). \tag{7}$$

Additionally, the volumetric mass source of evaporation can be obtained by:

$$\dot{m}''' = \frac{K \nabla T}{h_{fg}} \cdot \nabla C. \tag{8}$$

Here h_{fg} is the latent heat of vaporization, K is the thermal conductivity and T indicates the temperature field. Since the mass flux is dependent on ∇C, the gas volume generated by evaporation is increased by increasing the density ratio as a result of Eq. (7). In order to decrease the maximum value of ∇C and provide a balance in estimating the evaporation and boiling speed, the interface thickness should increase as the density ratio increases. Hence, 3, 4 and 5 lattice unit interface thicknesses are set for density ratios of 10, 100 and 1000, respectively. Cahn and Hilliard assumed that the volume

diffusive flow rate is proportional to the chemical potential gradient $\nabla\mu$ as:

$$j = -M\nabla\mu, \tag{9}$$

where $M>0$ is the mobility factor.

The interactions between the liquid-gas interface and solid surface appear in the surface integral of the total free energy $(\psi_b+\psi_s)$ and is obtained as follows [18]:

$$\psi_b+\psi_s = \int\left(E_0(C)+\frac{k}{2}|\nabla C|^2\right)dV + \int \phi_0-\phi_1 C_s+\phi_2 C_s^2-\phi_3 C_s^2+\cdots\Big)dS. \tag{10}$$

Here, $E_0=\beta C^2(C-1)^2$ is the bulk energy, β is a constant, k is the gradient parameter, C_s is the composition at a solid surface and ϕ_i with $i=0,1,2,\ldots$ are the constant coefficients. By relating the mixing energy of an isothermal system to its composition, Lee [18] proposed the following equation for the chemical potential μ:

$$\mu = \mu_0 - k\nabla^2 C, \tag{11}$$

where μ_0 can be obtained from $\mu_0=\partial E_0/\partial C$. By combining Eqs. (5) and (9), the continuity equation reads as:

$$\frac{\partial C}{\partial t}+\nabla\cdot(uC) = \nabla\cdot(M\nabla\mu)-\frac{\dot{m}'''}{\rho_l}. \tag{12}$$

It is noted that in the case of divergence free velocity field, the volumetric mass source of evaporation vanishes and Eq. (12) reduces to the classical Cahn–Hilliard equation.

2.2. Three-dimensional discrete Boltzmann equations

The discrete form of Boltzmann equation of a non-ideal fluid can be written as:

$$\frac{Df_\alpha}{Dt} = \left(\frac{\partial}{\partial t}+e_\alpha\cdot\nabla\right)f_\alpha = -\frac{1}{\lambda}\left(f_\alpha - f_\alpha^{eq}\right)+\frac{1}{c_s^2}(e_\alpha-u)\cdot F\Gamma_\alpha, \tag{13}$$

$$f_\alpha^{eq} = w_\alpha\rho\left[1+\frac{e_\alpha\cdot u}{c_s^2}+\frac{(e_\alpha\cdot u)^2}{2c_s^4}-\frac{(u\cdot u)}{2c_s^2}\right], \tag{14}$$

where f_α and f_α^{eq} are particle and equilibrium distribution functions, respectively, e_α is the αth-direction microscopic particle velocity, and $c_s=c/\sqrt{3}$ is a lattice speed of sound with $c=\delta x/\delta t$ being the lattice speed. Here δx and δt are the lattice spacing and time step, respectively. Furthermore, λ is the relaxation time and $\Gamma_\alpha=f_\alpha^{eq}/\rho$. For three-dimensional simulations presented in this work, 19-velocity model (see Fig. 1), known as D3Q19, is chosen. The weighting coefficients, w_α, for these 19 directions are given by $w_0=1/3$, $w_{1\sim6}=2/36$ and $w_{7\sim18}=1/36$. The discrete velocity vector, e_α, for either direction is also set as:

$$(e_0,e_1,e_2,e_3,e_4,e_5,e_6,e_7,e_8,e_9,e_{10},e_{11},e_{12},e_{13},e_{14},e_{15},e_{16},e_{17},e_{18}=$$
$$\begin{bmatrix} 0 & 1 & 0 & -1 & 0 & 0 & 0 & 1 & -1 & -1 & 1 & 1 & 1 & -1 & -1 & 0 & 0 & 0 & 0 \\ 0 & 0 & 1 & 0 & -1 & 0 & 0 & 1 & 1 & -1 & -1 & 0 & 0 & 0 & 0 & 1 & 1 & -1 & -1 \\ 0 & 0 & 0 & 0 & 0 & 1 & -1 & 0 & 0 & 0 & 0 & 1 & -1 & -1 & 1 & 1 & -1 & -1 & 1 \end{bmatrix} \tag{15}$$

In Eq. (13), F represents the intermolecular force and reads as:

$$F = \rho c_s^2 - \nabla p - C\nabla\mu(C), \tag{16}$$

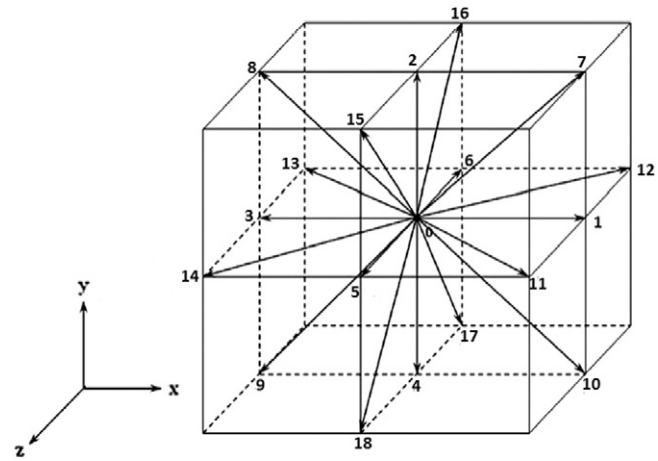

Fig. 1. Discrete velocity model (D3Q19).

where p is the dynamic pressure to enforce the incompressibility. In order to consider body source effects, one can add the following source term to the previous equation:

$$F_B = \begin{cases} g(\rho_l-\rho_v) & \rho_l \neq 0 \\ 0 & \rho_l = 0 \end{cases}, \tag{17}$$

where g is the gravitational acceleration.

Eq. (13) is the discrete Boltzmann equation (DBE) for obtaining the mass and momentum distribution functions. A new distribution function, g_α, transforms this equation into a DBE for the evolution of pressure and momentum:

$$g_\alpha = f_\alpha c_s^2 + (p_1-\rho c_s^2)\Gamma_\alpha(0). \tag{18}$$

Therefore, the new equilibrium distribution function g_α^{eq} is defined as:

$$g_\alpha^{eq} = f_\alpha^{eq}c_s^2+(p-\rho c_s^2)\Gamma_\alpha(0) = w_a\left[p+\rho c_s^2\left(\frac{e_\alpha.u}{c_s^2}+\frac{(e_\alpha.u)^2}{2c_s^4}-\frac{(u.u)}{2c_s^2}\right)\right] \tag{19}$$

Safari and Rahimian [19] defined an additional distribution function $h_\alpha=(C/\rho)f_\alpha$, for capturing the interface. Here, the modified DBEs for g_α and h_α, originally reported in [21], are adopted for our three-dimensional simulations as:

$$\frac{\partial g_\alpha}{\partial t}+e_\alpha\cdot\nabla g_\alpha = -\frac{1}{\lambda}\left(g_\alpha-g_\alpha^{eq}\right)+(e_\alpha-u)\cdot\left[\nabla\rho c_s^2(\Gamma_\alpha-\Gamma_\alpha(0))-C\nabla\mu\Gamma_\alpha\right] + \rho c_s^2\dot{m}'''\left(\frac{1}{\rho_v}-\frac{1}{\rho_l}\right)\Gamma_\alpha(0) \tag{20}$$

and

$$\frac{\partial h_a}{\partial t}+e_a\cdot\nabla h_a = \frac{c}{p}\left[-\frac{1}{\lambda}\left(f_a-f_a^{eq}\right)+\frac{(e_a-u)\cdot F}{c_s^2}\right]\Gamma_\alpha = -\frac{1}{\lambda}\left(h_\alpha-h_a^{eq}\right)+(e_\alpha-u) \times\left[\nabla C-\frac{C}{\rho c_s^2}(\nabla p+C\nabla\mu)\right]\Gamma_\alpha+\left(M\nabla^2\mu-\frac{\dot{m}'''}{\rho l}\right)\Gamma_\alpha. \tag{21}$$

By applying the trapezoidal rule, the following discrete forms for modified momentum and composition distribution functions ($\bar{g}_\alpha$ and $\bar{h}_\alpha$) can be derived:

$$\begin{aligned}\bar{g}_\alpha(x+e_\alpha\delta t,t+\delta t)-\bar{g}_\alpha(x,t) = &-\frac{1}{\tau+0.5}\left(\bar{g}_\alpha-\bar{g}_\alpha^{eq}\right)\big|_{(x,t)}+\delta t(e_\alpha-u)\\ &\times\left[\nabla\rho c_s^2(\Gamma_\alpha-\Gamma_\alpha(0))-C\nabla\mu\Gamma_\alpha\right]_{(x,t)}\\ &+\frac{\delta t}{2}\rho c_s^2\dot{m}'''\left(\frac{1}{\rho v}-\frac{1}{\rho l}\right)\Gamma_\alpha(0)\Big|_{(x,t)}\\ &+\frac{\delta t}{2}\rho c_s^2\dot{m}'''\left(\frac{1}{\rho v}-\frac{1}{\rho l}\right)\Gamma_\alpha(0)\Big|_{(x+e_\alpha\delta t,t+\delta t)}\end{aligned} \tag{22}$$

$$\begin{aligned}\bar{h}_\alpha(x+e_\alpha\delta t,t+\delta t)-\bar{h}_\alpha(x,t) = &-\frac{1}{\tau+0.5}\left(\bar{h}_\alpha-\bar{h}_\alpha^{eq}\right)\Big|_{(x,t)}+\delta t(e_\alpha-u)\\ &\times\left[\nabla C-\frac{C}{\rho c_s^2}(\nabla p+C\nabla\mu)\right]\Gamma_\alpha\Big|_{(x,t)}\\ &+\frac{\delta t}{2}\left(M\nabla^2\mu-\frac{\dot{m}'''}{\rho l}\right)\Gamma_\alpha\Big|_{(x,t)}\\ &+\frac{\delta t}{2}\left(M\nabla^2\mu-\frac{\dot{m}'''}{\rho l}\right)\Gamma_\alpha\Big|_{(x+e_\alpha\delta t,t+\delta t)}\end{aligned} \tag{23}$$

where τ is the nondimensional relaxation time $\tau=\lambda/\delta t$ and is obtained by evaluating the kinematic viscosity $v=\tau c_s^2\delta t$ [18]. Additionally, the gradient and laplacian terms for the hypothetical quantity $\emptyset$ are equal to:

$$\frac{\partial\emptyset}{\partial X_i}=\sum\nolimits_{\alpha\neq0}\frac{w_\alpha e_\alpha.\hat{i}\left[\emptyset(x+e_\alpha\delta_t)-\emptyset(x-e_\alpha\delta_t)\right.}{2{c_s}^2\delta_t}, \tag{24}$$

$$\frac{\partial^2\emptyset}{\partial {X_i}^2}=\sum\nolimits_{\alpha\neq0}\frac{w_\alpha\left[\emptyset(x+e_\alpha\delta_t)-2\emptyset(x)+\emptyset(x-e_\alpha\delta_t)\right.}{{c_s}^2{\delta_t}^2}, \tag{25}$$

in which $\hat{i}$ is the unit vector pointing along the ith-coordinate axis (i.e. x, y or z axis). The convective diffusion equation for the temperature field can be solved with a separate distribution function, s_α, here defined as:

$$\frac{\partial s_\alpha}{\partial t}+e_\alpha.\nabla s_\alpha=-\frac{1}{\lambda_T}\left(s_\alpha-s_\alpha^{eq}\right) \tag{26}$$

with a new equilibrium distribution function s_α^{eq}:

$$s_\alpha^{eq}=w_\alpha T\left(1+\frac{e_\alpha.u}{{c_s}^2}\right). \tag{27}$$

The discrete form of Eq. (26) reads as:

$$s_\alpha(x+e_\alpha\delta t,t+\delta t)-s_\alpha(x,t)=-\frac{\left(s_\alpha-s_\alpha^{eq}\right)}{2\tau_T}\Big|_{x+e_\alpha\delta t,t+\delta t}-\frac{\left(s_\alpha-s_\alpha^{eq}\right)}{2\tau_T}\Big|_{x,t}, \tag{28}$$

where $\tau_T=\lambda_T/\delta t$ is the nondimensional relaxation time and is obtained by considering the thermal diffusion coefficient $\alpha=c_s^2\tau_T\delta t$. Thus the modified distribution function $\bar{s}_\alpha$ is defined as:

$$\bar{s}_\alpha(x,t)=s_\alpha(x,t)+\frac{s_\alpha(x,t)-s_\alpha^{eq}(x,t)}{2\tau_T}. \tag{29}$$

Finally, the macroscopic fluid and flow properties can be computed using the zero and first order moments of modified distribution functions as follows:

$$C=\sum_\alpha\bar{h}_\alpha \tag{30}$$

$$\rho u=\frac{1}{c_s^2}\sum_\alpha e_\alpha\bar{g}_\alpha-\frac{\delta t}{2}C\nabla\mu \tag{31}$$

$$p=\sum_\alpha\bar{g}_\alpha+\frac{\delta t}{2}u\cdot\nabla\rho c_s^2 \tag{32}$$

$$T=\sum_\alpha\bar{s}_\alpha. \tag{33}$$

Here, Eqs. (30) to (33) are used to compute composition, momentum, pressure and temperature, respectively.

3. Result and discussion

3.1. Code verification and model validation

The pressure difference across the interface of a static spherical droplet under the surface tension force, without and with evaporation condition (i.e. the evaporation of static droplet) is used for validating the accuracy of the proposed three-dimensional multiphase model. These test cases are used to evaluate the Laplace law and the evaporation d^2 law, respectively. The computational domain for this test case is a cube with $N_x\times N_y\times N_z=100\times100\times100$ grid points with the initial liquid droplet radius of 20 lattice units. The simulations are performed for the constant density ratio of $\rho_l/\rho_v=1000$ and the surface tension of $\sigma=0.0001$ [N/m]. The outflow boundary condition is considered at the cubic faces. At the initial time step, a uniform temperature field inside the droplet and surrounding vapor are fixed to be T_{sat} and T_{gas}, respectively. A schematic of computational domain and boundary conditions of static droplet evaporation is illustrated in Fig. 2.

For the first test case, quiescent droplets with different radii are generated inside the computational domain. There is no temperature gradient at the interface. Therefore, Stefan number, defined as the ratio of sensible heat to the latent heat $st=c_{pg}(T_{gas}-T_{sat})/h_{fg}$, is equal to zero and the droplet radius remains constant. Under this condition, the pressure difference across the droplet interface should follow the Laplace law. Fig. 3 presents the pressure difference across the droplet interface under the influence of the surface tension force for several droplet radiuses, R. As can be seen the numerical results are in good agreement with the analytical solution confirming the accuracy of the code for quiescent droplets.

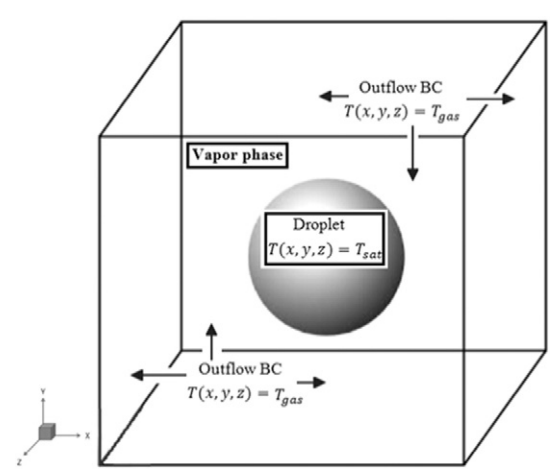

Fig. 2. Computational domain and boundary conditions of the vaporizing droplet simulation ($\rho_l/\rho_v=1000$ and $N_x\times N_y\times N_z=100\times100\times100$).

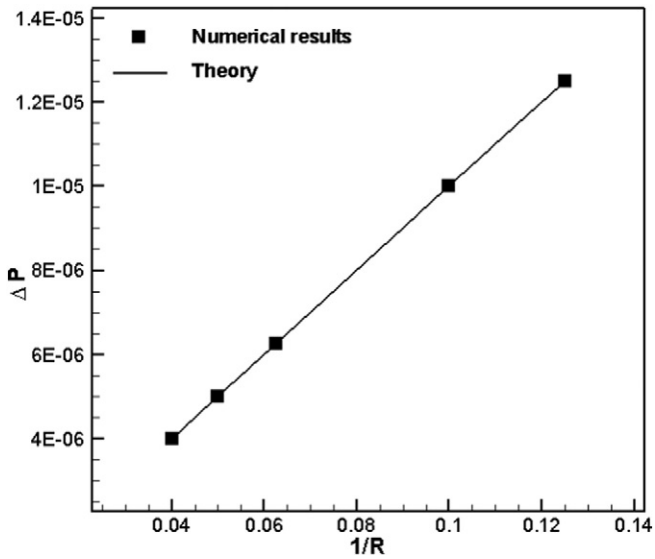

Fig. 3. The comparison of numerically computed pressure difference as a function of inverse droplet radius with the Laplace's law for the static spherical droplet with $\sigma = 0.0001$ [N/m]. and $\rho_l/\rho_v = 1000$.

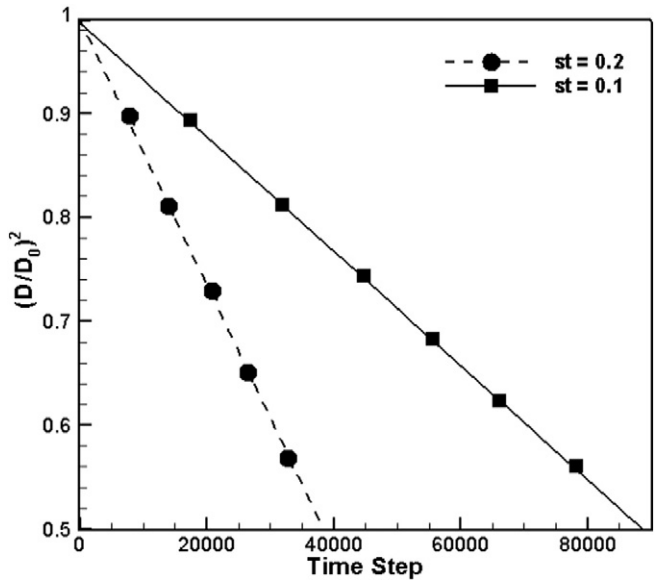

Fig. 5. The variation of non-dimensional squared diameter as a function of time step for two Stefan numbers (evaporation d^2 law problem).

For the second test case, the evaporation is initiated by the temperature gradient at the interface, i.e. $T_{gas} > T_{sat}$. Therefore, the radius of spherical droplet is reduced due to the evaporation. Contours of velocity magnitude (in lattice units) and velocity vectors at the box mid-plane after 20,000 time steps are presented in Fig. 4. The time variations of the dimensionless droplet diameter for two different Stefan numbers namely, st = 0.1 and st = 0.2, are plotted in Fig. 5. As expected, the droplet evaporation rate increases with increasing the Stefan number. Additionally, the squared diameter ratio and as a consequence the droplet area reduces linearly with time satisfying the evaporation d^2law.

3.2. Computational domain of bubble growth in pool boiling

A cubic domain is used for the simulation of pool boiling in the current work (see Fig. 6). The bounce back boundary conditions for momentum and composition distribution functions $\overline{g}_\alpha$ and $\overline{h}_\alpha$ are applied at the bottom surface. A second order extrapolation is implemented for the evaluation of unknown distribution function at the lateral boundaries. This is done based on the value of the distribution functions on the first and the second evaluation point layers inside of the fluid. No mass flux at the solid boundaries, necessitates zero chemical potential gradients in the normal direction:

$$n \cdot \nabla \mu|_s = 0, \tag{34}$$

where n is the unit vector normal to the surface. Another boundary condition is obtained by neglecting the terms higher than second order in ψ_s and minimizing the total energy $(\psi_s + \psi_b)$ against C:

$$n \cdot \nabla C\Big|_s = -\frac{\phi_1}{k} \tag{35}$$

The angle between liquid-vapor interfaces and solid wall is called contact angle and is given as a boundary condition in the present study. Briant [33] proposed a partial wetting model based on free energy Boltzmann method. According to Young's law, this angle is calculated as:

$$\cos\theta_w = \frac{\sigma_{SG} - \sigma_{SL}}{\sigma_{GL}} = \frac{(1+\Omega)^{\frac{3}{2}} - (1-\Omega)^{\frac{3}{2}}}{2} \tag{36}$$

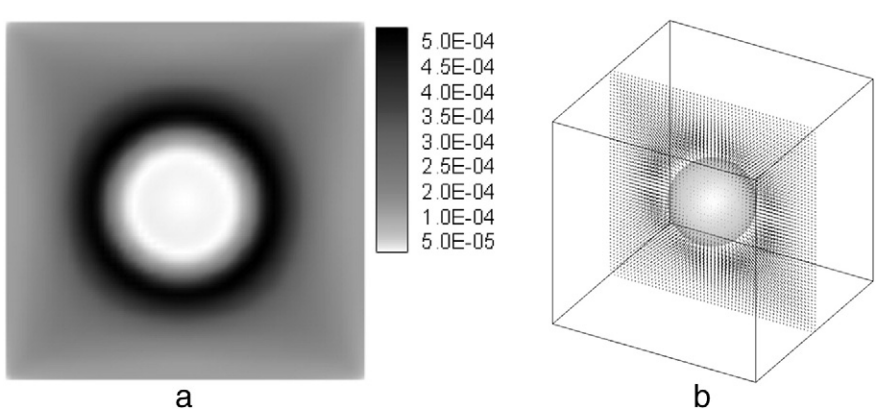

Fig. 4. (a) Contours of velocity magnitude (in lattice units) and (b) velocity vectors at the time step 20,000. Here, $\sigma = 0.0001$[N/m], $\rho_l/\rho_v = 1000$, $st = 0.2$ and $R_0 = 20$ lattice unit.

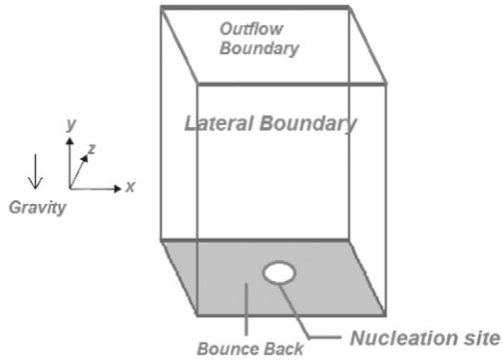

Fig. 6. Schematic of computational domain

with

$$\Omega = \phi_1 / \sqrt{2k\beta} \tag{37}$$

where θ_w is a contact angle and is measured from the liquid side. σ_{SG} and σ_{SL} are the solid-gas and solid-liquid surface tension respectively (the contact angle is assumed to be 93.1 in this work) and also Ω is known as wetting parameter.

An outflow boundary condition is set at the upper side of the computational domain. A constant temperature is applied on the bottom surface. The effect of gravity acceleration is presented by applying a density dependent body force in the vertical direction. In the following calculations, a density ratio of $\rho_l/\rho_v = 1000$ is applied. A spherical bubble with the radius of two-lattice unit is rested at the center of superheated wall domain.

3.3. Convergence study

The only way to gain confidence in the adequacy of grid resolution is to conduct a mesh refinement study. Therefore, in this section, a convergence study for the current numerical study is performed. The simulation results of two different meshes are compared. We have investigated the effect of lateral interaction between bubble and boundary condition on the bubble growth and its departure for two different mesh sizes namely, $40 \times 40 \times 70$ and $80 \times 80 \times 140$, in order to make sure that the domain size and mesh resolution have minimum effects on the bubble departure diameter and its dynamics. Boundary conditions for two grid resolutions are identical.

As can be seen in Fig. 7-a the coarse mesh result is almost identical with the fine one in the stage of bubble departure when the bubble diameter is smaller than half of domain lateral size. However, lateral interactions have some effects in the stage of bubble separation (Fig. 7-b). Therefore, it is better to use the fine mesh in the latter stage. Since the simulation results of both meshes in the bubble growth stage and before its separation is the same (i.e. has no effect on departure diameter, shape and time), we perform our simulation in domain sizes $40 \times 40 \times 70$ for the sake of time and memory optimization.

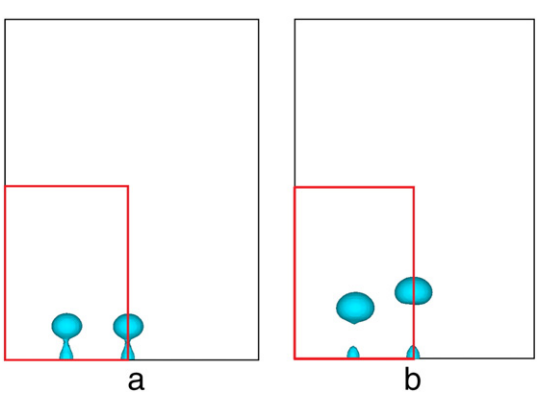

Fig. 7. Domain size effect using two different resolutions ($40 \times 40 \times 70$ and $80 \times 80 \times 140$) with $\rho_l/\rho_v = 1000$, $Ja = 0.0092$, $\sigma = 0.002$ and $g = 0.006$.

3.4. Pool boiling on a horizontal superheated wall

Figs. 8 and 9 present the single bubble time evolution and their corresponding temperature profiles over time, respectively. As can be seen in Fig. 8 vapor bubble grows in a nearly spherically shape on the superheated wall. The bubble nucleus attaches to the wall since the volume of bubble is small. At this stage the surface tension is dominant. During time, the bubble grows and its volume increases. Eventually, the bubble develops to a point where it detaches from its stem due to the buoyancy force.

It is noted that the bubble diameter increases rapidly until it reaches the stage of separation, then the upward movement of bubble slows down when the bubble neck is formed. Afterward, the entire vapor mass separates into two parts of different sizes where the upper part gets away from the superheated surface. Comparing with Mukherjee and Kandlikar [34], it can be seen that the process of bubble growth as well as its three-dimensional buoyant topology are in good agreement with the experimental results of single bubble growth. This confirms the accuracy of the current three-dimensional lattice Boltzmann model presented in this work.

Fig. 9 shows the temperature field evolution of the rising bubble while it grows. It can be seen that the bubble is superheated with an initially non-uniform temperature field. Afterward, when the bubble leaves the wall, the temperature reaches to the value that is slightly below the saturation temperature. This behavior is in good agreement with the experimental thermal interferometric patterns and two-dimensional non-isothermal lattice Boltzmann results presented, respectively, in [30] and [21]. It is noted that most of the previous multiphase lattice Boltzmann studies were not able to predict the temperature field inside the bubble where it is assumed to be constant [28,29]. However, from this figure it is illustrated that the modified Lee's method presented in the current study is capable of predicting the temperature field inside and outside the bubble successfully.

3.5. Bubble departure diameter

To further validate the presented three-dimensional model, effects of different parameters including, Jacob number, gravity acceleration (g) and surface tension (σ) on the bubble departure diameter are studied in this part.

One of the most widely used correlations for the relation between the bubble departure diameter (D) and physical parameters including gravitational acceleration and surface tension (σ) is proposed by Fritz [35]:

$$D = 0.0208\theta\sqrt{\frac{\sigma}{g(\rho_l - \rho_v)}}, \tag{38}$$

where θ is the bubble contact angle with the surface. Kocamustafaogullari and Ishii [36] modified this expression in the following form:

$$D = 2.64 \times 10^{-5}\sqrt{\frac{\sigma}{g(\rho_l - \rho_v)}}\left(\frac{\rho_l - \rho_v}{\rho_v}\right)^{0.9}. \tag{39}$$

It is noted that this correlation is independent of the contact angle. Gorenflo et al. [37] proposed an experimental correlation which includes the effect of thermal diffusivity of liquid (α_l) as well as Jacob

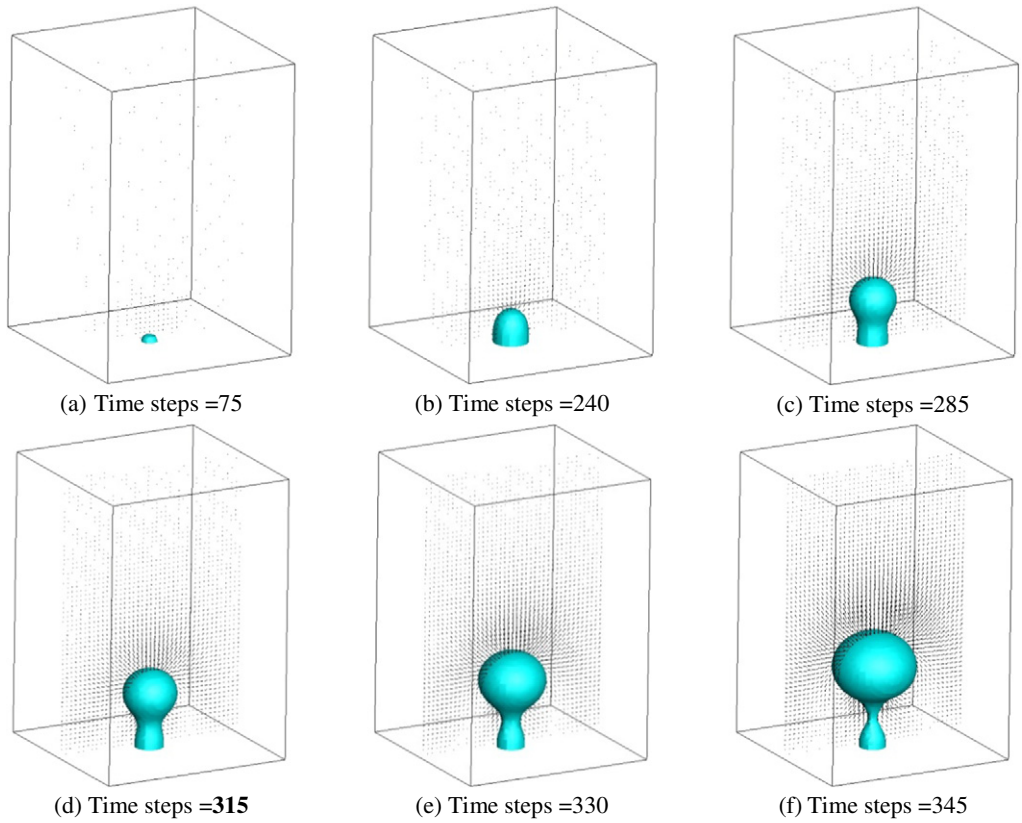

Fig. 8. Single bubble growth on a superheated wall before detachment ($\rho_l/\rho_v = 1000$, $Ja = 0.0185$, $\sigma = 0.002$ and $g = 0.006$).

number (Ja):

$$D = C_1\left(\frac{Ja^4\alpha_l^2}{g}\right)^{1/3}\left[1+\sqrt{1+\frac{2\pi}{3Ja}}\right]^{4/3}, \tag{40}$$

where $\pi = 3.14$ and C_1 is a liquid dependent constant.

Kocamustafaogullari [36] and Fritz [35] suggested that the bubble departure diameter varies with $g^{-0.5}$, however, in Gorenflo's correlation [37] the bubble departure is a function of $g^{-0.334}$.

The effect of gravity acceleration on the bubble departure diameter is presented in Fig. 10. It is observed that the bubble departure diameter increases with decreasing the gravity acceleration. This decrement is proportional to $g^{-0.354}$ which is in mesh with the correlation proposed

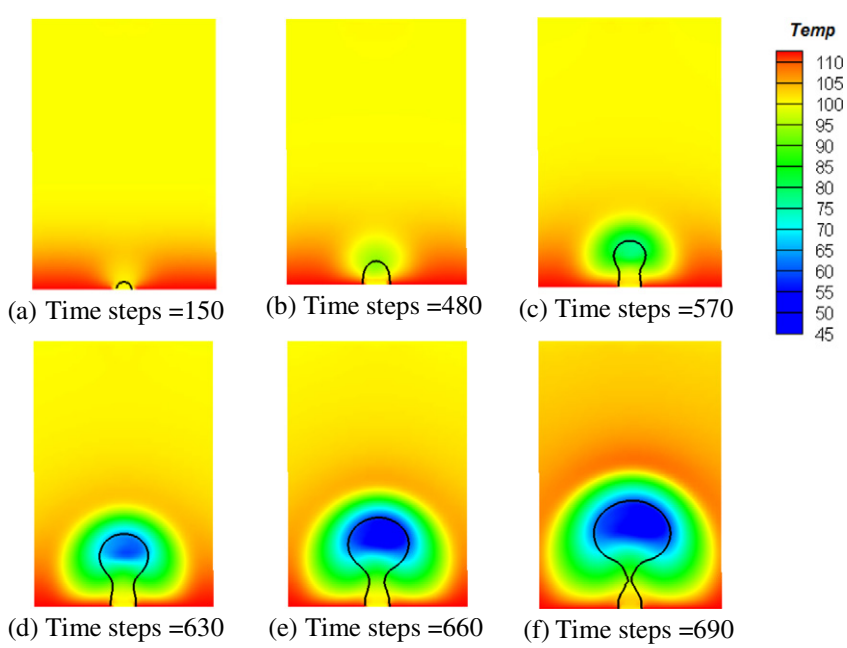

Fig. 9. Single bubble temperature profile over time ($\rho_l/\rho_v = 1000$, $Ja = 0.0185$, $\sigma = 0.002$ and $g = 0.006$).

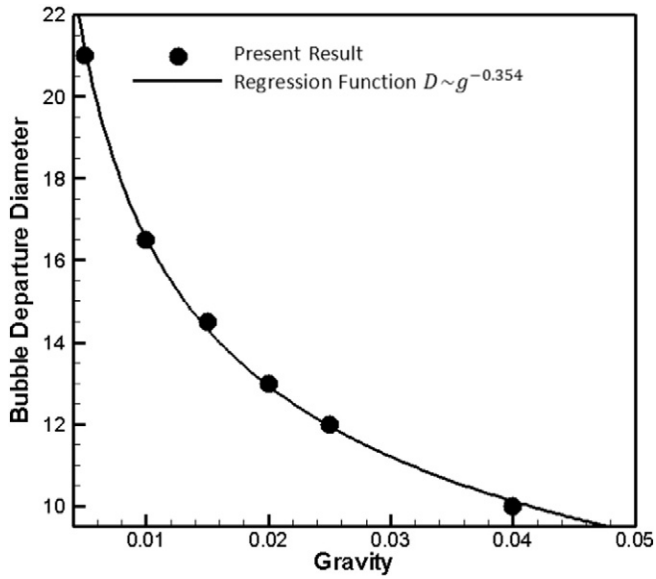

Fig. 10. Effect of gravity *acceleration* on the bubble departure diameter ($\rho_l/\rho_v = 1000$, $Ja = 0.0185$, $\sigma = 0.002$).

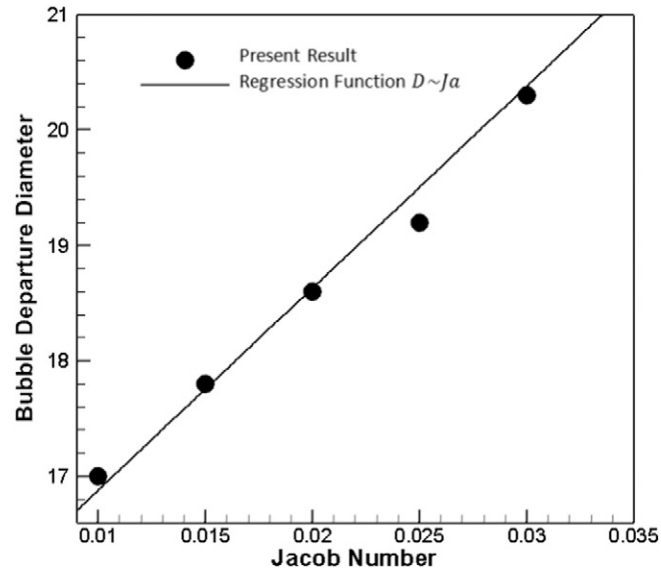

Fig. 12. Effect of the Jacob number on the bubble departure diameter ($\rho_l/\rho_v = 1000$, $\sigma = 0.002$ and $g = 0.006$).

by Gorenflo [37]. This is in contradiction with the recent lattice Boltzmann results presented in [35,36] where the authors found the dependency of $g^{-0.5}$ for their bubble departure diameter. It is noted that the latter (correlation presented by Gorenflo [37]) takes the effect of Jacob number, the ratio of sensible to latent energy absorbed during liquid-vapor phase change, into account; therefore, one may expect more accurate predictions from this correlation when compared with its counterparts presented in Fritz [35] and Kocamustafaogullari's [36]. This further confirms the superior results drawn by the present model.

The effect of surface tension on the bubble departure diameter is presented in Fig. 11. The bubble departure diameter and surface tension have the proportionality of $\sigma^{0.5}$ which is in good agreement with Eqs. (38) and (39). Finally, Fig. 12 shows the effect of Jacob number on the bubble departure diameter. As expected, following Eq. (40), the bubble departure diameter increases linearly with increasing the Jacob number.

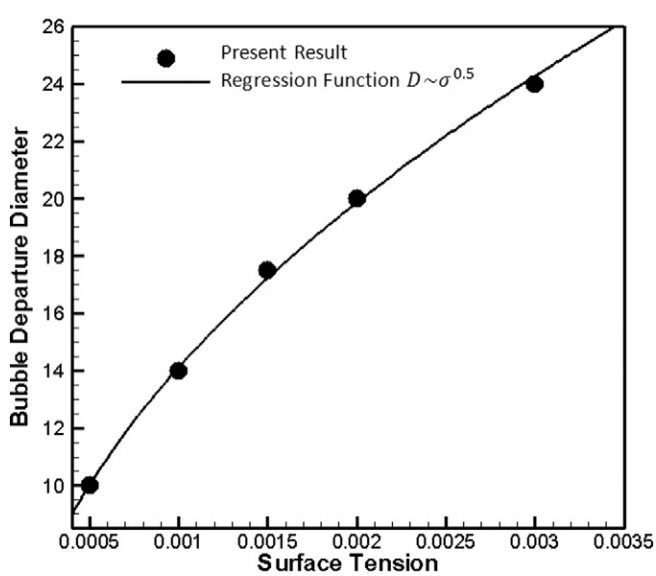

Fig. 11. Effect of surface tension on the bubble departure diameter ($\rho_l/\rho_v = 1000$, $Ja = 0.0185$, $g = 0.006$)

3.6. Multiple bubble departure

To further show the ability of the present model in capturing more complex physics, the simulation result of multiple bubble formation sites is shown in Fig. 13. As can be seen the air bubble rises due to the pressure difference between its top and bottom. The higher the pressure difference, the faster the rising velocity of the bubble. This creates an upward fluid jet at the center of the bubble. When the energy of this jet reaches a certain level, it is able to create a vortex ring around the bubble. If three sites of bubble columns are far enough apart to coalesce or have an effect on each other, their growing process is similar to that of a single bubble case in terms of the bubble departure diameter time and departure geometry. While, if the bubbles are close to each other, as it is in Fig. 13, the central bubble departure is delayed because of the vortex rings of the neighboring bubbles. The vortex rings of adjacent bubbles interact with the bubble in the middle and push it down which cause a postponement in the central bubble departure time. This phenomenon which is called micro-convection or bubble pumping, caused by bubble motion, is also reported in [25]. It is worth mentioning that although the micro-convection phenomenon causes a delay in the departure of the middle bubble, as seen in Fig. 13-c, it increases the heat transfer amount from the heated wall. It is noted that the physical and constant parameters in this simulation is the same as the single bubble formation problem presented in Section 3.3.

As can be seen in this figure the dynamic behavior of such system as well as complex physical phenomena such as micro convection and vortex ring mechanism on the bubble growth and bubble departures from superheated wall are predicted very well which further confirms the capability of presented model for capturing more complex phenomena.

4. Conclusion

In this article, a modified three-dimensional lattice Boltzmann multiphase model was presented and its feasibility for different pool boiling problems was investigated. The presented model was based on the modified multiphase Lee's model, which is capable of simulating the problems with high-density ratios. The three-dimensional multiphase model is validated against the analytical solution of evaporation d^2 law and Laplace's law. Then, the flow and temperature fields around

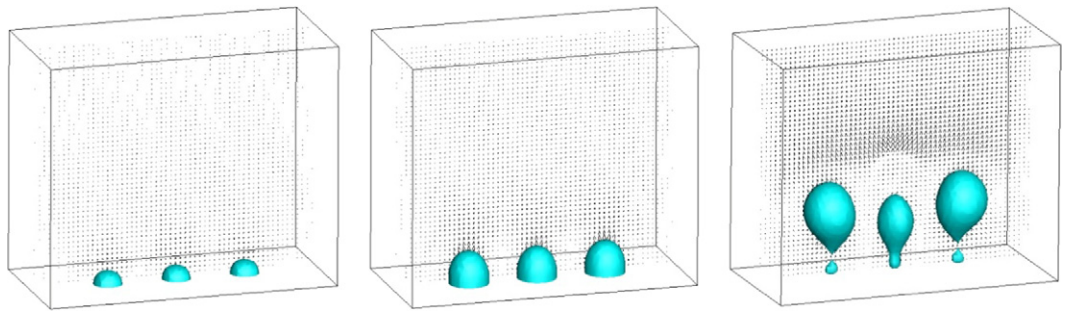

(a) Time steps =75 (b) Time steps=240 (c) Time steps =660

Fig. 13. Multi bubble growth and departure ($\rho_l/\rho_v = 1000$, $Ja = 0.0185$, $\sigma = 0.002$ and $g = 0.006$).

bubbles are obtained during the pool boiling process. We showed that the present model is capable of predicting the temperature field inside the bubble. The dynamic behavior of a single bubble was presented in order to further assess the accuracy of the present model. The bubble departure diameter was found to be proportional to gravitational acceleration and surface tension, respectively, as $g^{-0.354}$ and $\sigma^{0.5}$ which is consistent with available literature. Furthermore, the simulation results of bubble departure diameter were linearly proportional to the Jacob number, as predicted by Gorenflo [37]. Finally, the simulation of multiple bubble departure phenomena was performed to further show the capabilities of the presented model in capturing more complex physical phenomena such as micro-convection and vortex ring mechanism. The model will be used for simulation of more sophisticated physical systems in our future works.

References

[1] S.O. Unverdi, G. Tryggvason, A front-tracking method for viscous, incompressible, multi-fluid flows, J. Comput. Phys. 100 (1992) 25–37.
[2] C.W. Hirt, B.D. Nichols, Volume of fluid (VOF) method for the dynamics of free boundaries, J. Comput. Phys. 39 (1981) 201–225.
[3] R. Sadeghi, M. Safdari Shadloo, K. Hooman, Numerical investigation of the natural convection film boiling around elliptical tubes, Numer. Heat Transf. A Appl. (2016).
[4] D. Peng, B. Merriman, S. Osher, H. Zhao, M. Kang, A PDE-based fast local level set method, J. Comput. Phys. 155 (1999) 410–438.
[5] A. Rahmat, N. Tofighi, M. Shadloo, M. Yildiz, Numerical simulation of wall bounded and electrically excited Rayleigh–Taylor instability using incompressible smoothed particle hydrodynamics, Colloids Surf. A Physicochem. Eng. Asp. 460 (2014) 60–70.
[6] A. Zainali, N. Tofighi, M.S. Shadloo, M. Yildiz, Numerical investigation of Newtonian and non-Newtonian multiphase flows using ISPH method, Comput. Methods Appl. Mech. Eng. 254 (2013) 99–113.
[7] M.S. Shadloo, Improved Multiphase Smoothed Particle Hydrodynamics. PhD Thesis, Sabanci University, 2013.
[8] M.S. Shadloo, D. Le Touzé, G. Oger, Smoothed particle hydrodynamics method for fluid flows, towards industrial applications: motivations, current state, and challenges, Comput. Fluids 136 (2016) 11–34.
[9] R. Sadeghi, M.H. Rahimian, Simulation of bubble sonoluminescing phenomena with lattice Boltzmann method, Modares Mech. Eng. 15 (2015) 383–391.
[10] H. Huang, M. Sukop, X. Lu, Multiphase Lattice Boltzmann Methods: Theory and Application, John Wiley & Sons, 2015.
[11] A.K. Gunstensen, D.H. Rothman, S. Zaleski, G. Zanetti, Lattice Boltzmann model of immiscible fluids, Phys. Rev. A 43 (1991) 4320.
[12] X. Shan, H. Chen, Lattice Boltzmann model for simulating flows with multiple phases and components, Phys. Rev. E 47 (1993) 1815.
[13] M.R. Swift, E. Orlandini, W. Osborn, J. Yeomans, Lattice Boltzmann simulations of liquid-gas and binary fluid systems, Phys. Rev. E 54 (1996) 5041.
[14] A. Xu, Finite-difference lattice-Boltzmann methods for binary fluids, Phys. Rev. E 71 (2005) 066706.
[15] X. He, S. Chen, R. Zhang, A lattice Boltzmann scheme for incompressible multiphase flow and its application in simulation of Rayleigh–Taylor instability, J. Comput. Phys. 152 (1999) 642–663.
[16] T. Inamuro, T. Ogata, S. Tajima, N. Konishi, A lattice Boltzmann method for incompressible two-phase flows with large density differences, J. Comput. Phys. 198 (2004) 628–644.
[17] H. Zheng, C. Shu, Y.-T. Chew, A lattice Boltzmann model for multiphase flows with large density ratio, J. Comput. Phys. 218 (2006) 353–371.
[18] T. Lee, Effects of incompressibility on the elimination of parasitic currents in the lattice Boltzmann equation method for binary fluids, Comput. Math. Appl. 58 (2009) 987–994.
[19] H. Safari, M.H. Rahimian, M. Krafczyk, Consistent simulation of droplet evaporation based on the phase-field multiphase lattice Boltzmann method, Phys. Rev. E 90 (2014) 033305.
[20] T. Lee, C.-L. Lin, A stable discretization of the lattice Boltzmann equation for simulation of incompressible two-phase flows at high density ratio, J. Comput. Phys. 206 (2005) 16–47.
[21] A. Begmohammadi, M. Farhadzadeh, M.H. Rahimian, Simulation of pool boiling and periodic bubble release at high density ratio using lattice Boltzmann method, Int. Commun. Heat Mass Transf. 61 (2015) 78–87.
[22] M.A. Hatani, M. Farhadzadeh, M.H. Rahimian, Investigation of vapor condensation on a flat plate and horizontal cryogenic tube using lattice Boltzmann method, Int. Commun. Heat Mass Transf. 66 (2015) 218–225.
[23] N. Latifiyan, M. Farhadzadeh, P. Hanafizadeh, M.H. Rahimian, Numerical study of droplet evaporation in contact with hot porous surface using lattice Boltzmann method, Int. Commun. Heat Mass Transf. 71 (2016) 56–74.
[24] Z. Yang, T.-N. Dinh, R. Nourgaliev, B. Sehgal, Numerical investigation of boiling regime transition mechanism by a lattice–Boltzmann model, Nucl. Eng. Des. 204 (2001) 143–153.
[25] S. Ryu, S. Ko, Direct numerical simulation of nucleate pool boiling using a two-dimensional lattice Boltzmann method, Nucl. Eng. Des. 248 (2012) 248–262.
[26] S. Gong, P. Cheng, A lattice Boltzmann method for simulation of liquid–vapor phase-change heat transfer, Int. J. Heat Mass Transf. 55 (2012) 4923–4927.
[27] Q. Li, Q. Kang, M.M. Francois, Y. He, K. Luo, Lattice Boltzmann modeling of boiling heat transfer: the boiling curve and the effects of wettability, Int. J. Heat Mass Transf. 85 (2015) 787–796.
[28] D. Zhiqiang, L. Weizhong, S. Yongchen, A numerical investigation of bubble growth on and departure from a superheated wall by lattice Boltzmann method, Int. J. Heat Mass Transf. 53 (2010) 4916.
[29] T. Sun, W. Li, Three-dimensional numerical simulation of nucleate boiling bubble by lattice Boltzmann method, Comput. Fluids 88 (2013) 400–409.
[30] H. Beer, Das dynamische Blasenwachstum beim Sieden von Flüssigkeiten an Heizflächen, Forsch. Ingenieurwes. A 37 (1971) 85–90.
[31] E. Sattari, M. Delavar, E. Fattahi, K. Sedighi, Numerical investigation the effects of working parameters on nucleate pool boiling, Int. Commun. Heat Mass Transf. 59 (2014) 106–113.
[32] Q. Li, K. Luo, Q. Kang, Y. He, Q. Chen, Q. Liu, Lattice Boltzmann methods for multiphase flow and phase-change heat transfer, Prog. Energy Combust. Sci. 52 (2016) 62–105.
[33] A. Briant, Lattice Boltzmann simulations of contact line motion in a liquid-gas system, Philos. Trans. R. Soc. Lond. A Math. Phys. Eng. Sci 360 (2002) 485–495.
[34] A. Mukherjee, S.G. Kandlikar, Numerical study of single bubbles with dynamic contact angle during nucleate pool boiling, Int. J. Heat Mass Transf. 50 (2007) 127–138.
[35] W. Fritz, Maximum volume of vapor bubbles, Phys. Z. 36 (1935) 379–384.
[36] G. Kocamustafaogullari, Pressure dependence of bubble departure diameter for water, Int. Commun. Heat Mass Transf. 10 (1983) 501–509.
[37] D. Gorenflo, V. Knabe, V. Bieling, Bubble Density on Surfaces With Nucleate Boiling—Its Influence on Heat Transfer and Burnout Heat Fluxes at Elevated Saturation Pressures, Proceedings of 8th International Heat Transfer Conference 1986, pp. 1995–2000.